Evolution of Pattern Complexity in the Cahn-Hilliard Theory of Phase Separation

Marcio Gameiro

School of Mathematics

Georgia Institute of Technology

Atlanta, GA 30332, USA

Konstantin Mischaikow

Center for Dynamical Systems and Nonlinear Studies

Georgia Institute of Technology

Atlanta, GA 30332, USA

Thomas Wanner

Department of Mathematical Sciences

George Mason University

Fairfax, VA 22030, USA

July 3, 2004

Abstract

Phase separation processes in compound materials can produce intriguing and complicated patterns. Yet, characterizing the geometry of these patterns quantitatively can be quite challenging. In this paper we use computational algebraic topology to obtain such a characterization. Our method is illustrated for the complex microstructures observed during spinodal decomposition and early coarsening in both the deterministic Cahn-Hilliard theory, as well as in the stochastic Cahn-Hilliard-Cook model. While both models produce microstructures that are qualitatively similar to the ones observed experimentally, our topological characterization points to significant differences.

1 Introduction

The kinetics of phase separation in alloys has drawn considerable interest in recent years. Most alloys of commercial interest owe their properties to specific microstructures which are generated through special processing techniques, such as phase separation mechanisms. In quenched binary alloys, for example, one typically observes phase separation due to a nucleation and growth process, or alternatively, due to spinodal decomposition [3, 6, 7]. While the former process involves a thermally activated nucleation step, spinodal decomposition can be observed if the alloy is quenched into the unstable region of the phase diagram. The resulting inherent instability leads to composition fluctuations, and thus to instantaneous phase separation. Common to both mechanisms is the fact that the generated microstructures usually are thermodynamically unstable and will change in the course of time — thereby affecting the material properties. In order to describe these and other processes, one generally relies on models given by nonlinear evolution equations. Many of these models are phenomenological in nature, and it is therefore of fundamental interest to study how well the equations agree with experimental observations.

In this paper, we propose a comparison method based on the geometric properties of the microstructures. The method will be illustrated for the microstructures generated during spinodal decomposition. These structures are fine-grained and snake-like, as shown for example in Figure 1. The microstructures are computed using two different evolution equations which have been proposed as models for spinodal decomposition: The seminal Cahn-Hilliard model, as well as its stochastic extension due to Cook.

The first model for spinodal decomposition in binary alloys is due to Cahn and Hilliard [3, 6]; see also the surveys [5, 13]. Their mean field approach leads to a nonlinear evolution equation for the relative concentration difference $u = \varrho_A - \varrho_B$, where ϱ_A and ϱ_B denote the

relative concentrations of the two components, i.e., $\varrho_A + \varrho_B = 1$. The Ginzburg-Landau free energy is given by

$$E_\gamma(u) = \int_\Omega \left(\Psi(u) + \frac{\gamma}{2}|\nabla u|^2 \right) dx \, , \tag{1}$$

where Ω is a bounded domain, and the positive parameter γ is related to the root mean square effective interaction distance. The bulk free energy, Ψ, is a double well potential, typically

$$\Psi(u) = \frac{1}{4} \left(u^2 - 1 \right)^2 \, . \tag{2}$$

Taking the variational derivative $\delta E_\gamma / \delta u$ of the Ginzburg-Landau free energy (1) with respect to the concentration variable u, we obtain the chemical potential

$$\mu = -\gamma \Delta u + \frac{\partial \Psi}{\partial u}(u) \, ,$$

and thus the Cahn-Hilliard equation $\partial u / \partial t = \Delta \mu$, i.e.,

$$\frac{\partial u}{\partial t} = -\Delta \left(\gamma \Delta u - \frac{\partial \Psi}{\partial u}(u) \right) \, , \tag{3}$$

subject to no-flux boundary conditions for both μ and u. Due to these boundary conditions, any mass flux through the boundary is prohibited, and therefore mass is conserved. We generally consider initial conditions for (3) which are small-amplitude random perturbations of a spatially homogeneous state, i.e., $u(0, x) = m + \varepsilon(x)$, where ε denotes a small-amplitude perturbation with total mass $\int_\Omega \varepsilon = 0$. In order to observe spinodal decomposition, the initial mass m has to satisfy $(\partial^2 \Psi / \partial u^2)(m) < 0$.

One drawback of the deterministic partial differential equation (3) is that it completely ignores thermal fluctuations. To remedy this, Cook [8] extended the model by adding a

random fluctuation term ξ, i.e., he considered the stochastic Cahn-Hilliard-Cook model

$$\frac{\partial u}{\partial t} = -\Delta \left(\gamma \Delta u - \frac{\partial \Psi}{\partial u}(u) \right) + \sigma \cdot \xi , \tag{4}$$

where

$$\langle \xi(t,x) \rangle = 0 , \qquad \langle \xi(t_1,x_1)\xi(t_2,x_2) \rangle = \delta(t_1 - t_2)q(x_1 - x_2) .$$

Here $\sigma > 0$ is a measure for the intensity of the fluctuation and q describes the spatial correlation of the noise. In other words, the noise is uncorrelated in time. For the special case $q = \delta$ we obtain space-time white noise, but in general the noise will exhibit spatial correlations. See also [19].

Both the deterministic and the stochastic model produce patterns which are qualitatively similar to the microstructures observed during spinodal decomposition [4]. Recent mathematical results for (3) and (4) have identified the observed microstructures as certain random superpositions of eigenfunctions of the Laplacian, and were able to explain the dynamics of the decomposition process in more detail [2, 23, 24, 28, 29, 32].

Even though both models are based on deep physical insight, they are phenomenological models. Many researchers have therefore studied how well the models agree with experimental observations. See for exampe [1, 11, 14, 25], as well as the references therein. Most of these studies have been restricted to testing scaling laws. Exceptions include for example Ujihara and Osamura [31], who perform a quantitative evaluation of the kinetics by analyzing the temporal evolution of the scattering intensity of small angle neuron scattering in Fe-Cr alloys. Another approch was pursued by Hyde et al. [15], who consider spinodal decomposition in Fe-Cr alloys. Using experimental data obtained by an atom probe field ion microscopy PoSAP analysis, they study whether the observed microstructures are topologically equivalent to the structures generated by several model equations.

Two structures are considered topologically equivalent, if one can be deformed into the other without cutting or gluing. While it is difficult in general to determine when two structures are equivalent, one can easily obtain a measure for the degree of similarity by studying topological invariants. These are objects (such as numbers, or other algebraic objects) assigned to each structure, which remain unchanged under deformations. In other words, if these invariants differ for two structures, the structures cannot be topologically equivalent. Yet, similarities between the invariants indicate similarities between the considered structures.

The topological invariant used in [15] is the number of handles in the microstructure occupied by one of the two material phases. This number is computed using techniques from digital topology [18]. These techniques are indirect in nature and compute the number of handles by relating it to the Euler characteristic of the structure, which can be computed easily in three space dimensions. As the authors point out, "designing a computer program to directly count the handle density in a complex structure would be extremely difficult [15, p. 3419]." Recent progress in computational homology has resulted in such a program [16, 17].

In the remainder of this paper, we illustrate how the software package CHomP [17] can be used to quantify the pattern morphology generated by the deterministic Cahn-Hilliard model (3) and the stochastic model (4). To simplify the presentation, we only consider two-dimensional microstructures generated by spinodal decomposition, see again Figure 1. Nevertheless, the presented software works in arbitrary dimensions. Aside from the study of 3D microstructures, this also allows for the analysis of spatio-temporal structure changes, by including time as a fourth dimension. This method has been used in [10] to detect spatio-temporal chaos.

2 Numerical Solution of the Stochastic Model

We begin with a brief description of the numerical method used for approximating the Cahn-Hilliard-Cook equation (4). In order to simplify the presentation, we only discuss the case of a one-dimensional base domain $\Omega = (0,1)$. The higher-dimensional situation can be treated analogously.

The deterministic part of the evolution equation (4) is approximated using a finite difference scheme with linearly implicit time-stepping. To this end, we choose a time step Δt and a spatial grid size N, and let $\Delta x = 1/N$. For any $k \in \mathbb{N}$ we let $t_k = k \cdot \Delta t$ and approximate the solution $u(t_k, \cdot)$ of (4) by the N-vector $U(t_k) = (U_1(t_k), \ldots, U_N(t_k))$, where $U_n(t_k) \approx u(t_k, x_n)$ with $x_n = 1/(2N) + (n-1)/N$ for $n = 1, \ldots, N$. The second derivative with respect to x is approximated using standard divided differences, i.e., the values of $u_{xx}(t, \cdot)$ are approximated by $LU(t)$, where L denotes the appropriate tridiagonal matrix. With this notation the numerical method for (4) can be written as

$$\frac{U(t_{k+1}) - U(t_k)}{\Delta t} = -\frac{\varepsilon^2}{\Delta x^4} \cdot L^2 U(t_{k+1}) - \frac{1}{\Delta x^2} \cdot Lf(U(t_k)) + \sigma \cdot \xi(t_k) \,,$$

which is equivalent to the linear system

$$\left(I + \frac{\varepsilon^2 \Delta t}{\Delta x^4} L^2 \right) U(t_{k+1}) = U(t_k) - \frac{\Delta t}{\Delta x^2} \cdot Lf(U(t_k)) + \sigma \cdot \Delta t \cdot \xi(t_k) \,. \tag{5}$$

The numerical approximation of the noise term will be specified below. This scheme is a variation of linearly implicit schemes, as discussed for example in [12, 26]. In contrast to the methods described in these references, we only split off the bi-Laplacian part of the right-hand side. This ensures the invertibility of the matrix $(I + (\varepsilon^2 \Delta t/\Delta x^4) \cdot L^2)$, regardless of the step size Δt. At the same time, we can still choose considerably larger step sizes than in

the explicit case. See in particular Quarteroni and Valli [26, Section 12.2.2], where a method analogous to ours is analyzed.

We now turn our attention to the approximation of the noise term. The stochastic forcing term ξ in (4) is given as the generalized derivative of an infinite-dimensional Wiener process $W(t)$, $t \geq 0$, which can be written as

$$W(t) = \sum_{\ell=1}^{\infty} \alpha_\ell \cdot \beta_\ell(t) \cdot \varphi_\ell \,. \tag{6}$$

In this series representation, the stochastic processes β_ℓ denote independent real-valued Brownian motions, and the functions φ_ℓ, $\ell \geq 0$, are the eigenfunctions of the Laplacian on Ω subject to homogeneous Neumann boundary conditions. Notice that the sum in (6) excludes the constant eigenfunction φ_0. This is necessary to ensure that the stochastic Cahn-Hilliard equation remains mass conserving. The noise process $\xi = \partial_t W$ then satisfies

$$\Delta t \cdot \xi(t_k) \approx W(t_{k+1}) - W(t_k) = \sum_{\ell=1}^{\infty} \alpha_\ell \cdot (\beta_\ell(t_{k+1}) - \beta_\ell(t_k)) \cdot \varphi_\ell \,. \tag{7}$$

The definition of Brownian motion implies that the random variable $\beta_\ell(t_{k+1}) - \beta_\ell(t_k)$ is normally distributed with mean 0 and variance $t_{k+1} - t_k = \Delta t$. Therefore, the scaled random variable $(\beta_\ell(t_{k+1}) - \beta_\ell(t_k))/\sqrt{\Delta t}$ is normally distributed with mean 0 and variance 1. As in [30], the series in (7) is approximated by its projection onto the span of the first $N - 1$ eigenfunctions $\varphi_1, \ldots, \varphi_{N-1}$. Altogether, we approximate the noise term ξ by

$$\Delta t \cdot \xi(t_k) \approx \sum_{\ell=1}^{N-1} \alpha_\ell \cdot (\beta_\ell(t_{k+1}) - \beta_\ell(t_k)) \cdot \varphi_\ell = \sqrt{\Delta t} \cdot \sum_{\ell=1}^{N-1} \alpha_\ell \cdot B_\ell \cdot \varphi_\ell \,, \tag{8}$$

where the B_ℓ denote independent normally distributed random variables with mean 0 and standard deviation 1. Equations (5) and (8) constitute our numerical approximation of the

evolution equation (4).

The above numerical scheme can be implemented efficiently using the fast Fourier trans-
form. One can show that the eigenvectors of the tridiagonal matrix L can be obtained by
evaluating the above-defined eigenfunctions φ_ℓ at each entry of the vector $x = (x_1, \ldots, x_N)$.
The time-consuming part in the algorithm is the solution of a linear system of the form
$AU = V$ at every timestep, where $A = I + (\varepsilon^2 \Delta t / \Delta x^4) \cdot L^2$. Thus, by transforming the
vector V into Fourier space using the discrete cosine transform, dividing component-wise
by the eigenvalues of A, and then applying the inverse discrete cosine transform, the linear
system $AU = V$ can be solved in time $O(N \log N)$. Notice that the noise approximation
can easily be added to this scheme, before applying the inverse cosine transform. This is the
reason for choosing the upper limit of the sum (8) as $N - 1$, instead of N.

The above description can easily be generalized to the two-dimensional situation. The
simulations in this paper used an implementation in C in combination with the fast Fourier
transform package FFTW [9]. Moreover, we consider the case of cut-off noise, i.e., in (6)
we choose $\alpha_\ell = 1$ for $\ell = 1, \ldots, N - 1$, and $\alpha_\ell = 0$ for $\ell \geq N$. This guarantees a spatial
correlation function q which closely approximates δ.

3   Homology

As is indicated in the introduction we claim that homology provides a useful technique for
identifying and distinguishing the evolving microstructures of (3) and (4). While this paper
is clearly not the appropriate forum for an in depth description of algebraic topology and
homology three points do need to be discussed: (1) what structures do we want to understand
the geometry of, (2) what geometric features does homology measure, and (3) how is the
homology being computed?

Since we are interested in phase separation and $u(t, x)$ represents the relative concentration difference between the two materials at time t and location x, the simplest decomposition of the domain consists of the two sets

$$X^+(t) := \{x \in \Omega \mid u(t, x) > m\} \quad \text{and} \quad X^-(t) := \{x \in \Omega \mid u(t, x) < m\} \ , \qquad (9)$$

where m denotes a suitable threshold value, such as the total mass. In this situation, the sets $X^\pm(t)$ represent the regions in the material where one or the other element dominates. Of course, u is the solution of a (stochastic) nonlinear partial differential equation and hence we cannot expect to have an explicit representation of the sets $X^\pm$. As was indicated in Section 2 we use a finite difference scheme to numerically solve (3) and (4) and thus given the domain $\Omega = (0, 1) \times (0, 1)$ with a spatial grid size $N \times N$ we obtain values $U(t_k, x_\ell^1, x_n^2)$ where $x_j = 1/(2N) + (j - 1)/N$. We give a geometric interpretation to this numerical grid via the squares $Q_{\ell,n} := [(\ell - 1)/N, \ell/N] \times [(n - 1)/N, n/N]$. In particular we define a cubical approximation to $X^\pm(t)$ by

$$U^+(t_k) := \left\{Q_{\ell,n} \mid U(t_k, x_\ell^1, x_n^2) > m\right\} \quad \text{and} \quad U^+(t_k) := \left\{Q_{\ell,n} \mid U(t_k, x_\ell^1, x_n^2) < m\right\}$$

Figure 1 indicates sets $U^\pm(t_k)$ at various times steps for a particular solution to (3) and (4). It is easy to observe that patterns produced by $U^\pm(t_k)$ are complicated, time dependent, and appear at intermediate time steps to differ qualitatively for the deterministic and stochastic models. Before moving on to describe how homology can be used to quantify these observations, notice that if the computations had been performed in a three-dimensional domain, then the same approach could be used except that the 2-dimensional squares $Q_{\ell,n}$ would be replace by 3-dimensional cubes.

This leads us to the question of what geometric properties homology can measure. We

8

begin with the fact that for any topological space X there exist homology groups $H_i(X)$, $i = 0, 1, 2, \ldots$ (see [16] and the references therein). For a general space $H_i(X)$ takes the form of an arbitrary abelian group. However, in the context of our investigations there are two simplifying conditions. The first is that from the point of view of materials science we are only interested in structures that can occur in 3-dimensional Euclidean space. The second is that the spaces we compute the homology of are represented in terms of a finite number of cubes (squares if we restrict our attention to a 2-dimensional model as is being done in this paper). In this setting the homology groups are much simpler; first, $H_i(X) = 0$ for $i \geq 3$ and second, for $i = 0, 1, 2$,

$$H_i(X) \cong \mathbb{Z}^{\beta_i}$$

where $\mathbb{Z}$ denotes the integers and β_i is a non-negative integer called the i-th *Betti number*. Thus, for our purposes the homology groups are characterized by their Betti numbers.

Each of the homology groups measures a different geometric property. $H_0(X)$ counts the number of connected components (pieces) of the space X. More precisely, if $\beta_0 = k$, then X has exactly k components. A specific example of this is shown in the left diagram in Figure 2, where $\beta_0 = 26$ corresponding to the 26 different connected components. Observe that the size or the shape of the components does not play a role in the value of β_0. Depending on the application this can be taken as a strength or weakness of this approach. For the problems being discussed in this paper we see it as a strength, since we have no a priori knowledge of the specific geometry of the material microstructures.

$H_1(X)$, or more precisely β_1, provides a measure of the number of tunnels in the structure, though the correspondence is slightly more complicated. In a two-dimensional domain, such as that indicated in Figure 2, tunnels are reduced to loops. In particular, as is shown in the right diagram of Figure 2, the green structure encloses exactly four regions indicated by the

black curves and hence $\beta_1 = 4$. Notice that each of the remaining white regions hits the boundary. As before, size or shape plays no role in the definition of a loop.

For a three-dimensional structure loops become tunnels, where again the length or width of the tunnel is irrelevant. For example a washer has one wide but very short tunnel while a garden hose has a narrow but long tunnel. In either case $\beta_1 = 1$.

As mentioned earlier we are only considering a two-dimensional domain in which case $H_2(X) = 0$. However, for a general three-dimensional domain β_2 equals the number of enclosed volumes or cavities within the material.

We finish this section with a brief comment concerning the actual computation of the Betti numbers. As is indicated in the introduction this is done using the code CHomP [17]. An elementary introduction to homology and the underlying algorithms can be found in [16]. Typical computation times of the software in our situation are described in the next section.

4   Effects of Noise on the Pattern Morphology

In this section we use computational homology to study the effects of the stochastic forcing term in (4) on the temporal evolution of the pattern complexity. We consider the case of total mass $m = 0$ and Ψ as in (2), and restrict ourselves to $\gamma^{1/2} = 0.005$. The simulations are performed on the unit square $\Omega = (0,1) \times (0,1)$. For varying values of the noise intensity σ, we numerically integrate the Cahn-Hilliard-Cook equation (4) starting from a random perturbation of the homogeneous state $m = 0$ with amplitude 0.0001 up to time

$$t_{end} = \frac{160\gamma}{\Psi''(m)^2} \, , \qquad \text{where} \qquad \Psi''(m) = 3m^2 - 1 \, , \tag{10}$$

which in our situation reduces to $t_{end} = 0.004$. This time frame covers the complete spinodal decomposition phase, as well as early coarsening. The domain is discretized by a 512×512-

grid, the time interval $[0, t_{end}]$ is covered by $10,000$ integration steps. Every 50 time steps, the sets $X^{\pm}(t)$ introduced in the last section are determined, and finally their Betti numbers are computed using [17]. On a 2 GHz Dual Xeon Linux PC it took about 15 minutes to create the 402 sets $X^{\pm}(t)$ for $t/t_{end} = 0, 0.005, 0.010, \ldots, 0.995, 1$, as well as a total of 46 minutes to compute their Betti Numbers.

Figure 3 contains the results of these computations for two different values of the noise intensity. The solid red curves show the Betti number evolution for the deterministic case $\sigma = 0$, the dashed blue curves are for noise intensity $\sigma = 0.01$; the solution snapshots in Figure 1 are taken from these two simulations. At first glance, the graphs in Figure 3 are not surprising. For the initial time $t = 0$ both β_0 and β_1 are large, since the initial perturbation was chosen randomly on the computational grid. In fact, the actual values lie well outside the displayed range. The smoothing effect of (4) leads to a rapid decrease of the Betti numbers for times t close to 0, and coarsening behavior in the Cahn-Hilliard-Cook model is responsible for the decrease observed towards the end of the time window. All shown evolutions exhibit small-scale fluctuations, which are most likely artifacts caused by the cubical approximation of the sets $X^{\pm}(t)$. Even though these fluctuations are not necessarily desirable, they are a more or less automatic consequence of the numerical approximation of the partial differential equation (4).

Despite these similarities, there are some obvious differences between the deterministic and the stochastic evolution. In the deterministic situation, the initial complexity decay occurs sooner than in the stochastic case. In addition, it appears that the Betti numbers of $X^{+}(t)$ for $\sigma = 0.01$ decay more or less monotonically, provided we ignore the above-mentioned small-scale fluctuations. In contrast, in the deterministic case the initial decrease seems to be followed by a period of stagnation or even growth of the Betti numbers, see for example β_0 for $X^{+}(t)$ or β_1 for $X^{-}(t)$.

11

The observations made in the last paragraph could indicate fundamental differences between the deterministic and the stochastic Cahn-Hilliard model. However, these observations are based on a single randomly chosen initial condition, and it is therefore far from clear whether they represent behavior typical for either of the models. For this we have to observe ensembles of solutions for each of the models and study the statistics of their complexity evolutions. For the purposes of this paper, we concentrate on the averaged complexity evolution. Figure 4 shows the averaged Betti number evolution for six values of the noise intensity σ ranging from 0 to 0.01, in each case based on solution ensembles of size 100. The qualitative form of the complexity evolution curves differs substantially. For large noise the complexity decays monotonically, while it shows a surprising increase in the deterministic situation. The change between the two behaviors occurs gradually, and there seems to be a specific threshold σ_{cr} for the noise intensity beyond which monotone decay is observed. Notice also that despite the small ensemble size, the evolution curves of $X^+(t)$ and $X^-(t)$ are in good agreement, which for our choice of $m = 0$ and Ψ as in (2) has to be expected. In this sense, the ensemble behavior is a reflection of typical solution dynamics, reinforcing our above observations.

The simulations discussed so far consider the specific value $\gamma^{1/2} = 0.005$. We performed analogous simulations for various values of γ, for various grid sizes, and a variety of time steps. In each case, the time window extended from 0 to t_{end} as defined in (10). These results show that the behavior shown in Figure 4 is typical. In all cases, the time window covers the complete spinodal decomposition phase, as well as early coarsening; the resulting evolution curves for the deterministic case show the characteristic non-monotone behavior; for sufficiently large noise intensity we observe monotone decay. The only parameters changing with γ appear to be the absolute height of the evolution curves and the critical noise intensity σ_{cr}. While the height scaling will be addressed in more detail in the next section,

12

we close this section with a brief discussion of the dependence of σ_{cr} on γ.

To get a more accurate picture of the monotonicity properties of the evolution curves we compute the averaged Betti number evolution from larger solution ensembles and for times up to only $t_{end}/4$. As before, t_{end} is given by (10), and we consider the case $m = 0$. The noise intensity σ is chosen equal to $\gamma^{1/2}$, and the ensemble size is taken as $1,000$. The results of these simulations for $\gamma^{1/2} = 0.005$, 0.006, and 0.007 are shown in Figure 5. They indicate that the critical noise intensity σ_{cr} at which the monotonicity behavior of the evolution curves changes is given by

$$\sigma_{cr} \approx \gamma^{1/2} \; . \tag{11}$$

While we conjecture that (11) describes the correct scaling, verifying this conjecture is only possible by significantly increasing the computational effort. For larger values of ε one has to choose significantly larger ensemble sizes, due to the smallness of the Betti numbers. On the other hand, for smaller values of ε the spatial grid has to be refined considerably.

The results of this section demonstrate that Betti numbers can be used to quantitatively distinguish between microstructure morphologies generated by different models. Ultimately we hope that this quantitative information can be used to match models to actual experimental data. In fact, the limited experimental data in [15] seems to indicate that the handle density of the microstructures generated through spinodal decomposition decreases monotonically. Thus, these experimental results favor the stochastic Cahn-Hilliard-Cook model with squared noise intensities σ^2 larger than the interaction parameter γ.

5   Morphology Changes due to Mass Variation

So far we restricted our study to the case of equal mass, i.e., we assumed $m = 0$. Yet, spinodal decomposition can be observed as long as $\Psi''(m) < 0$, which for our choice of Ψ is equivalent

13

to $|m| < 3^{-1/2} \approx 0.577$. Total mass values outside this range lead to nucleation and growth behavior which produces microstructures consisting of isolated droplets — in contrast to the microstructures shown in Figure 1. In this section we use computational homology to quantify the pattern morphology changes during spinodal decomposition in the deterministic Cahn-Hilliard model (3) as the total mass is increased from $m = 0$ towards $m \approx 3^{-1/2}$.

Before presenting our numerical results, we have to address one technical issue. Even though the homogeneous state m is unstable as long as $\Psi''(m) < 0$, the strength of the instability changes with m. One can easily show that the growth rate of the most unstable perturbation of the homogeneous state is close to $\Psi''(m)^2/(4\gamma)$ [23]. Thus, as the total mass approaches the boundary of the spinodal region, the time frame for spinodal decomposition grows. In order to compare the pattern morphology for different values of the total mass we therefore scale the considered time window. As in the last section, we compute the solutions up to time t_{end} defined in (10), whose scaling is motivated by largest growth rate mentioned above.

How do changes in the total mass m affect the microstructures generated through spinodal decomposition? Figure 6 contains typical patterns for $m = 0, 0.1, \ldots, 0.5$. In each case, the pattern was generated by solving (3) up to time $t = 0.4 \cdot t_{end}$, with t_{end} as in (10). Notice that even though all of these microstructures are a consequence of phase separation through spinodal decomposition, the last two microstructures resemble the ones generated by nucleation and growth. In other words, Figure 6 indicates a gradual change from the highly interconnected structures observed in the equal mass case to the disconnected structures observed in nucleation.

In order to further quantify this gradual change, we use computational homology as in the last section. For $\gamma^{1/2} = 0.005$ and various values of m between 0 and 0.55 we computed the averaged Betti number evolution of the sets $X^{\pm}(t)$ in (9) from $t = 0$ up to time $t = t_{end}$.

14

The resulting two-dimensional surfaces are shown in Figure 7. To avoid the large Betti numbers close to the random initial state, these graphs do not include the times $t = 0$ and $t = 0.005 \cdot t_{end}$. Of particular interest is the topology of the sets $X^+(t)$ which correspond to the dominant phase. The graphs in the left column of Figure 7 show that in terms of the quantitative topological information given by the averaged Betti numbers, one observes a gradual and continuous change from the interconnected microstructures for $m = 0$ to the nucleation morphology. In addition, the graph of β_0 for $X^+(t)$ indicates that for $t/t_{end} > 0.25$, i.e., after the completion of spinodal decomposition, and for $m > 0.2$ the dominant phase forms a connected structure; that is, the complementary phase breaks up completely. Yet, the typical droplet structure reminiscent of nucleation and growth behavior can only be observed for values of the total mass larger than 0.3. In the surfaces of Figure 7 this is reflected by the fact that for fixed time t, the Betti number β_1 of the dominant phase $X^+(t)$ continues to increase with m until $m \approx 0.3$. As the total mass approaches $3^{-1/2}$, the first Betti number then decreases again, corresponding to an increasing droplet size.

Additional information can be obtained by combining the topological information for $X^+(t)$ with the information for the complementary sets $X^-(t)$. To illustrate this, consider again the microstructure in the left diagram of Figure 2 consisting of 26 components. Most of these components are introduced through boundary effects — only 6 components are internal. Even though the Betti number β_0 of $X^+(t)$ does not distinguish between these two types of components, only internal components of $X^+(t)$ introduce loops in $X^-(t)$. In other words, the first Betti number of $X^-(t)$ is a measure for the number of internal components of $X^+(t)$. Returning to Figure 7, this reasoning implies that internal components of $X^+(t)$ disappear at much smaller values of the total mass m than the value $m \approx 0.2$ stated above. In fact, for $m = 0, 0.025, 0.050, 0.075$, and 0.1 the average first Betti number of $X^-(t_{end})$ is given by 4.52, 2.16, 0.83, 0.32, and 0.07, respectively. For larger values of m it essentially

15

vanishes.

In addition to the results shown in Figure 7, we performed analogous simulations for $\gamma^{1/2} = 0.0025$, 0.0075, and 0.0100. In each case, the qualitative shape of the computed surfaces matched the one for $\gamma^{1/2} = 0.005$, only the absolute height of the surfaces changed. In fact, our computations indicate that the units on the vertical axes of Figure 7 scale proportionally to γ^{-1} for these values of γ.

The computations of this section indicate how homology can be used to quantify global morphological changes, such as connectivity, due to mass variation. They also indicate that by comparing different homological data, i.e., β_0 and β_1, inferences concerning the local structure of the material can be made. On a more general level, given a model of a particular material it would be interesting to seek correlations between macroscopic properties and the type of geometric information expressed in Figure 7. Comparisons of this nature would probably be of even greater importance in the case of three-dimensional simulations, since visualization of these phenomena would be extremely complicated.

6   Conclusion

In this paper we proposed the use of computational homology as an effective tool for quantifying and distinguishing complicated microstructures. Rather than discussing experimental data, we considered numerical simulations of the deterministic Cahn-Hilliard model, as well as its stochastic extension due to Cook. The obtained topological characterizations were used to (a) uncover significant differences in the temporal evolution of the pattern complexity during spinodal decomposition between the deterministic and the stochastic model, as well as to (b) establish the existence of a gradual transition of the spinodal decomposition microstructure morphology as the total mass approaches the boundary of the spinodal re-

gion. In order to simplify our presentation, the results were presented in a two-dimensional setting. Nevertheless, the computational tools are available for and effective in arbitrary dimensions.

We believe that the presented methods can serve as practical tools for assessing the quality of continuum models for phase separation processes in materials. This is achieved by providing quantitative topological information which can readily uncover differences in models as in (a). In addition, this quantitative information can be used to compare the computed microstructure topology to experimental observations. For example, the study in [15] determined the handle density of spinodally decomposing iron-chromium alloys. This quantity corresponds to the first Betti number, and the results of [15] indicate a monotone decay — which in combination with (a) favors the stochastic Cahn-Hilliard-Cook model over the deterministic one.

A second possible application is the identification of model parameters based on the microstructure topology. For example, our considerations in (b) resulted in characteristic evolution curves as a function of the parameter m, as well as in scaling information with respect to γ. Combined, these graphs could be used to determine specific values of these parameters for certain experimental situations.

It would be interesting to apply the methods presented in this paper to more elaborate models which include additional effects, such as for example anisotropic elastic forces [22] or polycrystalline structures [27]. Moreover, we believe that combining our methods with the matricity concept introduced in [20, 21] can further increase the classification potential of the method.

Acknowledgements

References

[1] K. Binder. Kinetics of phase separation. In L. Arnold, editor, *Stochastic Nonlinear Systems*, pages 62–71. Springer-Verlag, Berlin, 1981.

[2] D. Blömker, S. Maier-Paape, and T. Wanner. Spinodal decomposition for the Cahn-Hilliard-Cook equation. *Communications in Mathematical Physics*, 223(3):553–582, 2001.

[3] J. W. Cahn. Free energy of a nonuniform system. II. Thermodynamic basis. *Journal of Chemical Physics*, 30:1121–1124, 1959.

[4] J. W. Cahn. Phase separation by spinodal decomposition in isotropic systems. *Journal of Chemical Physics*, 42:93–99, 1965.

[5] J. W. Cahn. Spinodal decomposition. *Transactions of the Metallurgical Society of AIME*, 242:166–180, 1968.

[6] J. W. Cahn and J. E. Hilliard. Free energy of a nonuniform system I. Interfacial free energy. *Journal of Chemical Physics*, 28:258–267, 1958.

[7] J. W. Cahn and J. E. Hilliard. Free energy of a nonuniform system III. Nucleation in a two-component incompressible fluid. *Journal of Chemical Physics*, 31:688–699, 1959.

[8] H. Cook. Brownian motion in spinodal decomposition. *Acta Metallurgica*, 18:297–306, 1970.

[9] M. Frigo and S. G. Johnson. FFTW: An adaptive software architecture for the FFT. *Proc. ICASSP 1998*, 3:1381–1384, 1998.

[10] M. Gameiro, W. Kalies, and K. Mischaikow. Topological characterization of spatial-temporal chaos. *Preprint*, 2003.

[11] H. Garcke, B. Niethammer, M. Rumpf, and U. Weikard. Transient coarsening behaviour in the Cahn-Hilliard model. *Acta Materialia*, 51(10):2823–2830, 2003.

[12] E. Hairer and G. Wanner. *Solving Ordinary Differential Equations II*. Springer-Verlag, Berlin, 1991.

[13] J. E. Hilliard. Spinodal decomposition. In H. I. Aaronson, editor, *Phase Transformations*, pages 497–560. American Society for Metals, Metals Park, Ohio, 1970.

[14] J. M. Hyde, M. K. Miller, M. G. Hetherington, A. Cerezo, G. D. W. Smith, and C. M. Elliott. Spinodal decomposition in Fe-Cr alloys: Experimental study at the atomic level and comparison with computer models — II. Development of domain size and composition amplitude. *Acta Metallurgica et Materialia*, 43:3403–3413, 1995.

[15] J. M. Hyde, M. K. Miller, M. G. Hetherington, A. Cerezo, G. D. W. Smith, and C. M. Elliott. Spinodal decomposition in Fe-Cr alloys: Experimental study at the atomic level and comparison with computer models — III. Development of morphology. *Acta Metallurgica et Materialia*, 43:3415–3426, 1995.

[16] T. Kaczynski, K. Mischaikow, and M. Mrozek. *Computational Homology*, volume 157 of *Applied Mathematical Sciences*. Springer-Verlag, New York, 2004.

[17] W. Kalies and P. Pilarczyk. Computational homology program. www.math.gatech.edu/∼chom/, 2003.

[18] T. Y. Kong and A. Rosenfeld. Digital topology. Introduction and survey. *Computer Vision, Graphics and Image Processing*, 48(3):357–393, 1989.

[19] J. S. Langer. Theory of spinodal decomposition in alloys. *Annals of Physics*, 65:53–86, 1971.

[20] P. Leßle, M. Dong, and S. Schmauder. Self-consistent matricity model to simulate the mechanical behaviour of interpenetrating microstructures. *Computational Materials Science*, 15(4):455–465, 1999.

[21] P. Leßle, M. Dong, E. Soppa, and S. Schmauder. Simulation of interpenetrating microstructures by self-consistent matricity models. *Scripta Materialia*, 38(9):1327–1332, 1998.

[22] L. Löchte, A. Gitt, G. Gottstein, and I. Hurtado. Simulation of the evolution of GP zones in Al-Cu alloys: An extended Cahn-Hilliard approach. *Acta Materialia*, 48(11):2969–2984, 2000.

[23] S. Maier-Paape and T. Wanner. Spinodal decomposition for the Cahn-Hilliard equation in higher dimensions. Part I: Probability and wavelength estimate. *Communications in Mathematical Physics*, 195(2):435–464, 1998.

[24] S. Maier-Paape and T. Wanner. Spinodal decomposition for the Cahn-Hilliard equation in higher dimensions: Nonlinear dynamics. *Archive for Rational Mechanics and Analysis*, 151(3):187–219, 2000.

[25] M. K. Miller, J. M. Hyde, M. G. Hetherington, A. Cerezo, G. D. W. Smith, and C. M. Elliott. Spinodal decomposition in Fe-Cr alloys: Experimental study at the atomic level and comparison with computer models — I. Introduction and methodology. *Acta Metallurgica et Materialia*, 43:3385–3401, 1995.

[26] A. Quarteroni and A. Valli. *Numerical Approximation of Partial Differential Equations*. Springer-Verlag, Berlin, 1994.

[27] H. Ramanarayan and T. A. Abinandanan. Phase field study of grain boundary effects on spinodal decomposition. *Acta Materialia*, 51(16):4761–4772, 2003.

[28] E. Sander and T. Wanner. Monte Carlo simulations for spinodal decomposition. *Journal of Statistical Physics*, 95(5–6):925–948, 1999.

[29] E. Sander and T. Wanner. Unexpectedly linear behavior for the Cahn-Hilliard equation. *SIAM Journal on Applied Mathematics*, 60(6):2182–2202, 2000.

[30] T. Shardlow. Numerical methods for stochastic parabolic PDEs. *Numerical Functional Analysis and Optimization*, 20(1-2):121–145, 1999.

[31] T. Ujihara and K. Osamura. Kinetic analysis of spinodal decomposition process in Fe-Cr alloys by small angle neutron scattering. *Acta Materialia*, 48(7):1629–1637, 2000.

[32] T. Wanner. Maximum norms of random sums and transient pattern formation. *Transactions of the American Mathematical Society*, 356(6):2251–2279, 2004.
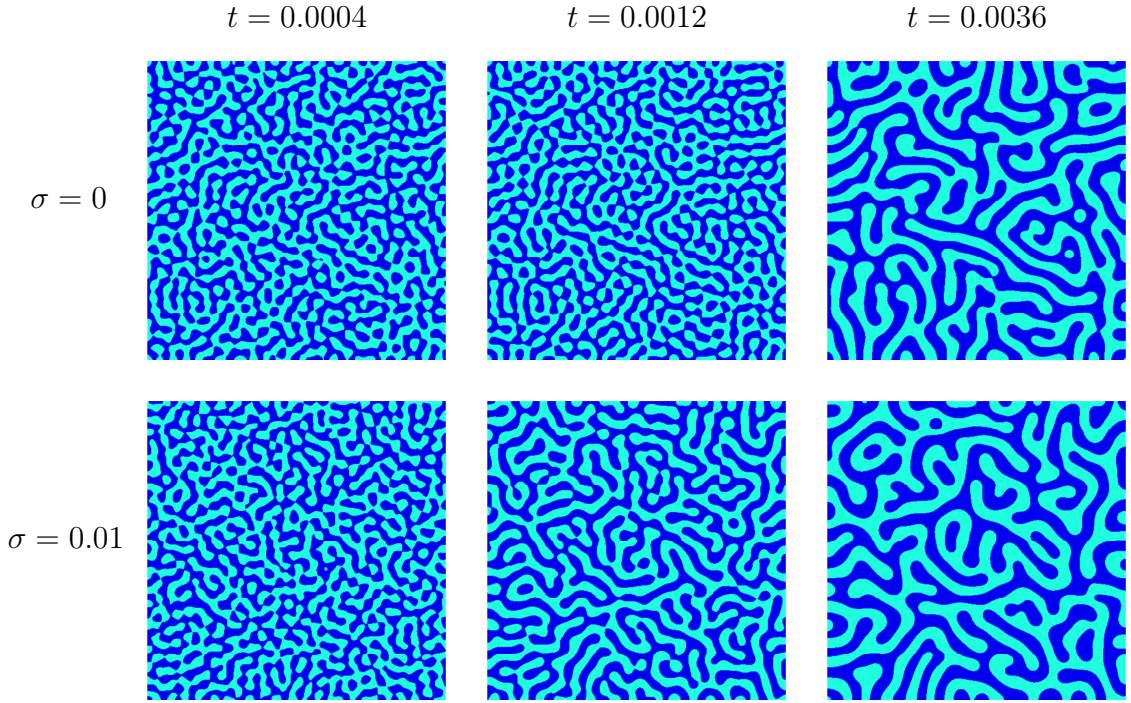
Figure 1: Microstructures obtained from the Cahn-Hilliard-Cook model (4). The top row shows solution snapshots for the deterministic case $\sigma = 0$, the bottom row is for noise intensity $\sigma = 0.01$. In both cases we used $\gamma^{1/2} = 0.005$ and $m = 0$. The set $X^+(t)$ defined in (9) is shown in dark blue.
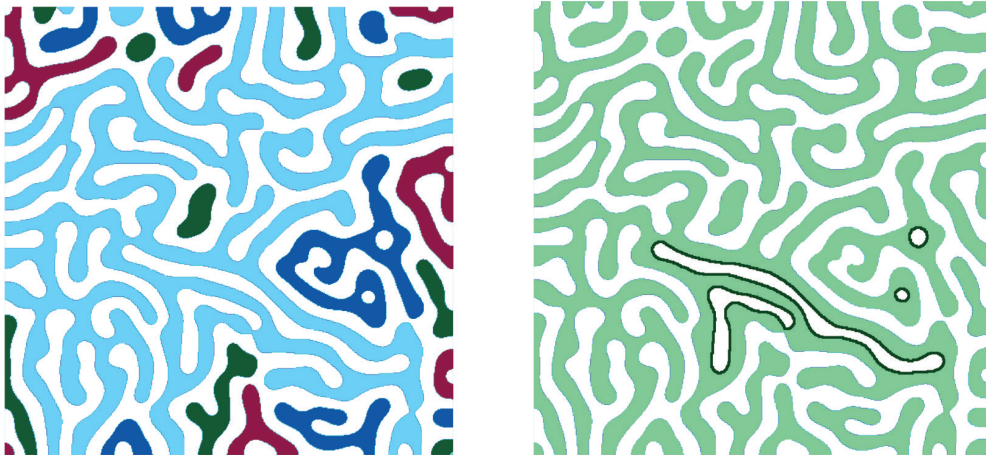

Figure 2: Betti numbers for the darker region of the $\sigma = 0$ and $t = 0.0036$ snapshot from Figure 1. The left diagram shows the $\beta_0 = 26$ components in different colors, the right diagram indicates the location of the $\beta_1 = 4$ loops.
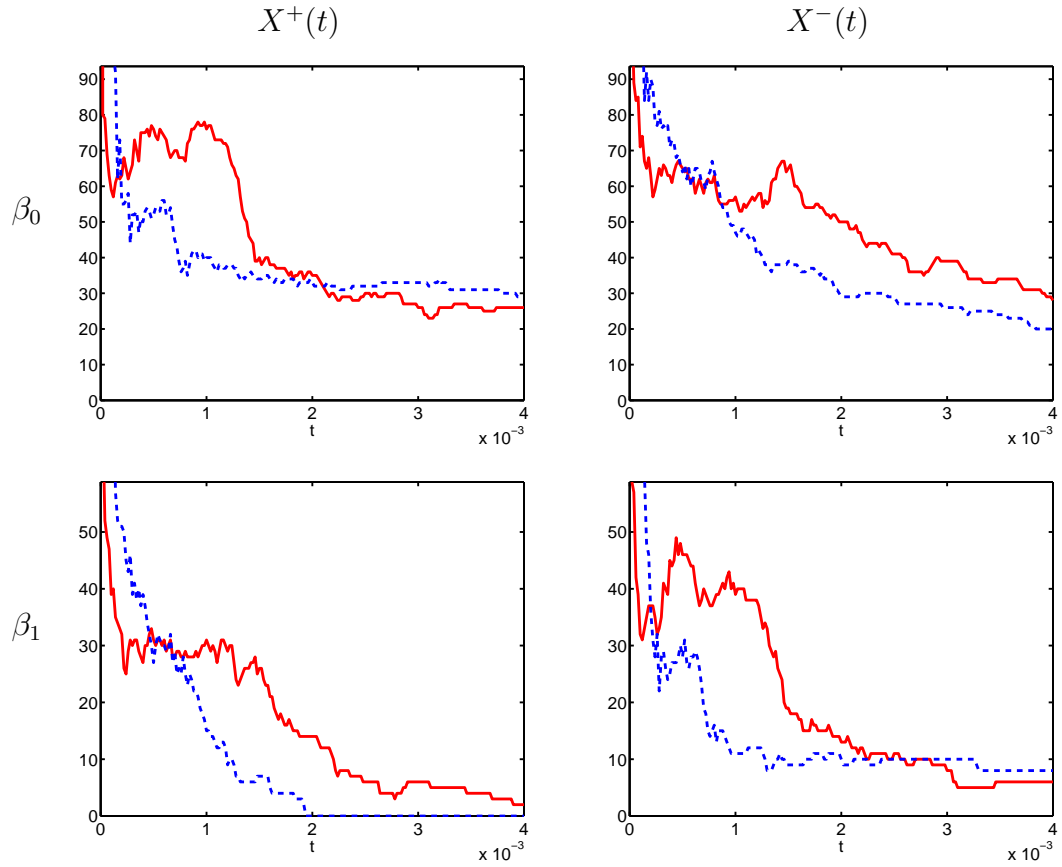
Figure 3: Evolution of the Betti numbers for the solutions of Figure 1. In each diagram, the solid red curve corresponds to $\sigma = 0$, the dashed blue curve is for $\sigma = 0.01$. In both cases we used $\gamma^{1/2} = 0.005$ and $m = 0$. The diagrams in the left column show the results for $X^{+}(t)$, the right column is for $X^{-}(t)$. The top row contains the evolutions of β_0, the bottom row shows β_1.
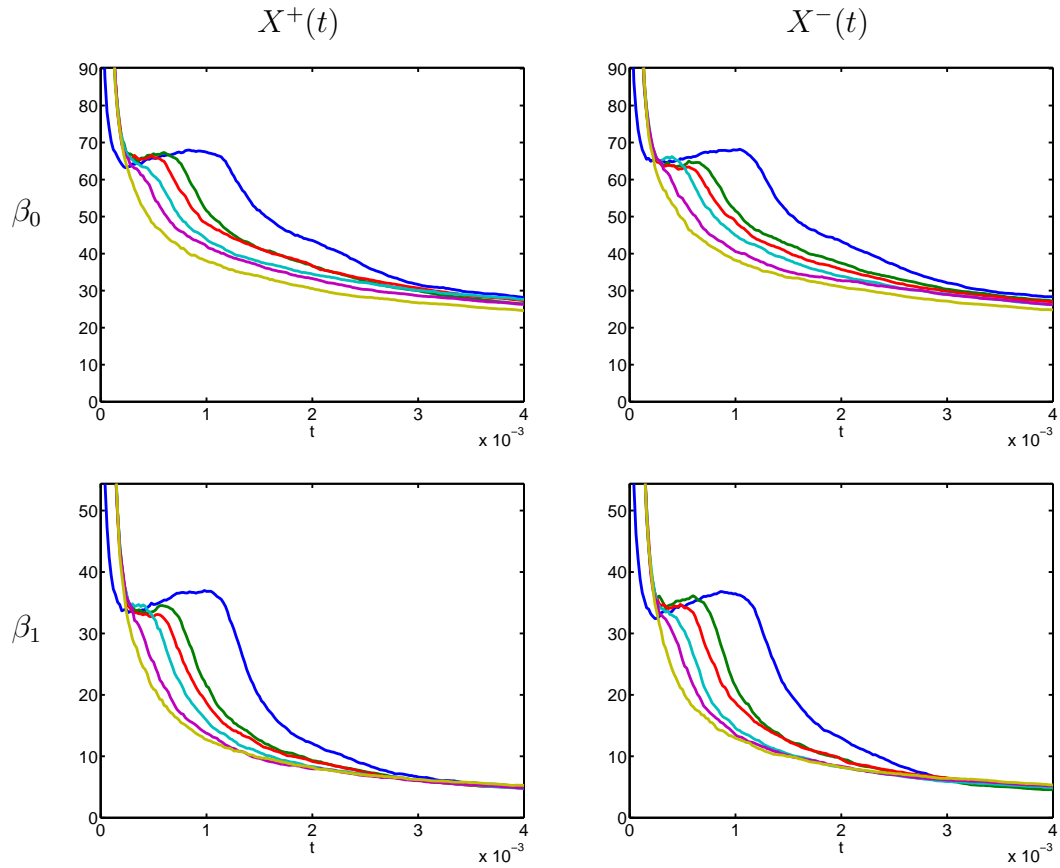
Figure 4: Evolution of Betti number averages for a sample size of 100, with $\gamma^{1/2} = 0.005$ and $m = 0$. In the top row at dimension level 60 the curves correspond to the values $\sigma = 0.1$, 0.03, 0.01, 0.003, 0.001, and 0, from left to right; analogously in the bottom row at level 25.
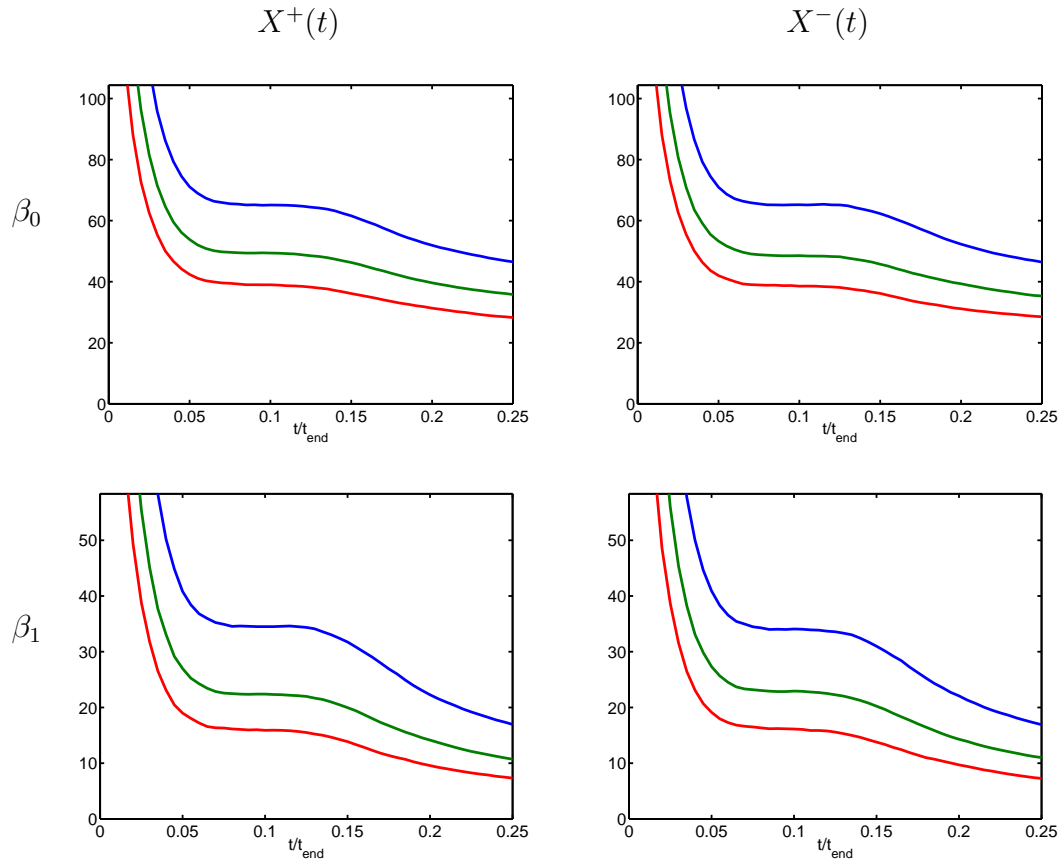
Figure 5: Evolution of Betti number averages for varying $\gamma^{1/2} = \sigma$ and $m = 0$. The blue (top), green (middle), and red (bottom) curves correspond to $\gamma^{1/2} = \sigma = 0.005, 0.006,$ and 0.007, respectively. The sample size for each of these simulations is $1,000$.
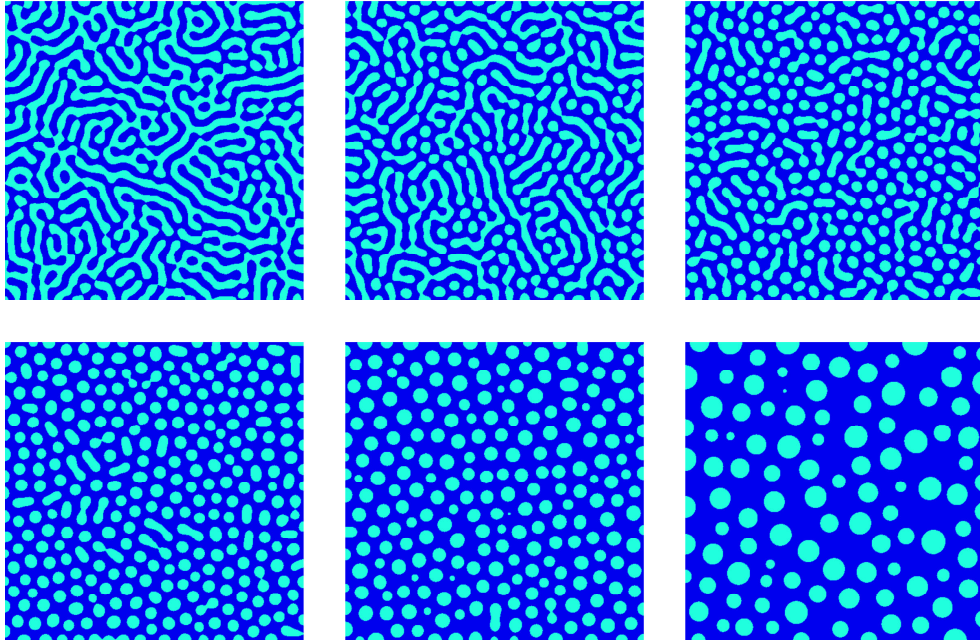
24

Figure 6: Microstructures obtained from the Cahn-Hilliard model (3) for $\gamma^{1/2} = 0.005$ for varying m. From top left to bottom right solution snapshots are shown for total mass $m = 0, 0.1, \ldots, 0.5$ at time $t = 0.4 \cdot t_{end}$, i.e., shortly after completion of the spinodal decomposition phase. The set $X^+(t)$ is shown in dark blue.
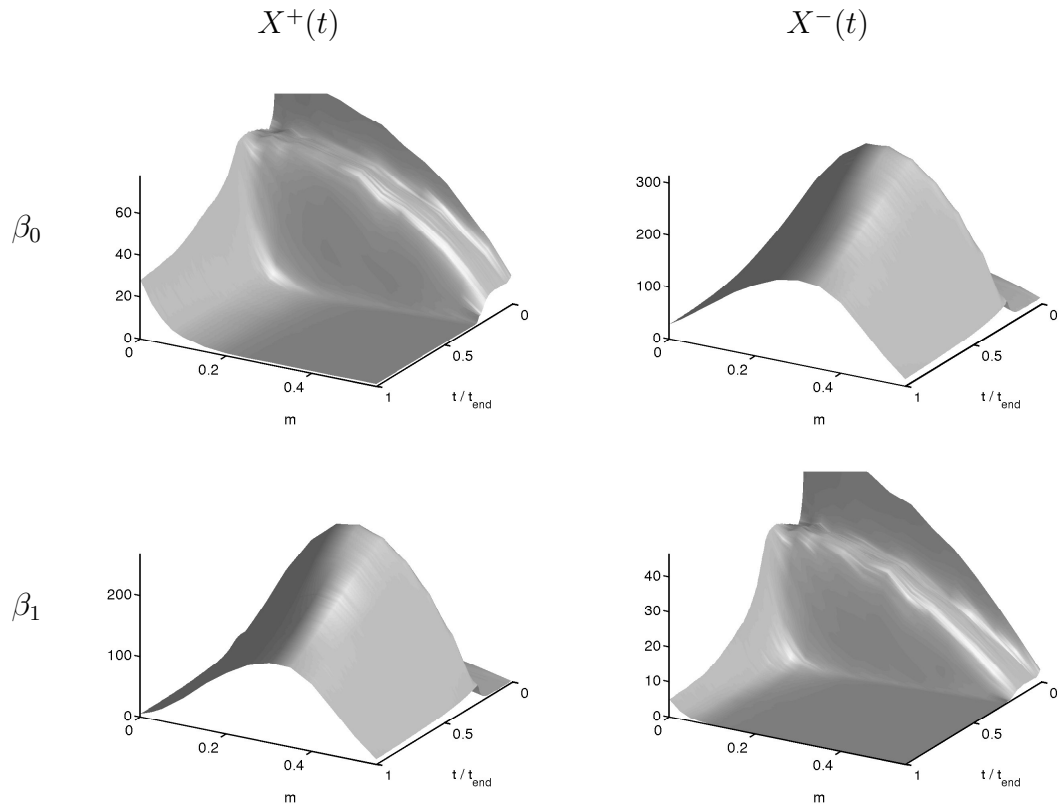
Figure 7: Evolution of Betti number averages for a sample size of 100, with $\gamma^{1/2} = 0.005$ and varying mass m. The left column corresponds to $X^+(t)$, the right one to $X^-(t)$; the top row contains the graphs for the 0-th Betti number, the bottom row for the first.